

Interface Properties in a Porous-Matrix Oxide Composite

Jared H. Weaver, Johann Rannou, Michael A. Mattoni, and Frank W. Zok[†]

Materials Department, University of California, Santa Barbara, California 93106-5050

This study focuses on the interfacial properties of a family of porous matrix oxide composites with uncoated fibers. Measurements of debond energy and sliding stress are made using a modified version of the established fiber push-in test. Modifications include the following: (i) use of a sphero-conical indenter (not a sharp-tipped one) to produce only elastic deformation of the fibers, and (ii) analysis of the loop width (instead of absolute displacements) to ascertain interface properties. The method obviates the need for indentation tests on reference (non-sliding) fibers. It also mitigates the problems associated with the elastic deformation of the surrounding matrix. The measured debond toughnesses (about 0.05 J/m²) are about two orders of magnitude lower than the fiber toughness. This ensures that debonding will occur when a matrix crack impinges on a fiber. Additionally, the sliding stresses are in the same range as those reported for C-coated Nicalon fibers in glass–ceramic matrices (about 5 MPa). The latter results are qualitatively consistent with the observed damage tolerance in these two seemingly disparate systems, as manifested in the degree of fiber pullout as well as the notch sensitivity of tensile strength.

I. Introduction

ENABLING damage tolerance through the use of porous matrices is now a well-established paradigm in high-performance oxide composites.^{1–10} From a mechanics perspective, the porosity serves two functions: (i) it reduces the energy release rate of matrix cracks relative to that in a dense matrix, and (ii) it leads to an inherently weak bond between the fibers and the matrix. Provided the matrix is sufficiently compliant and weak, the composite exhibits a high tensile strength and a low notch sensitivity,^{4,10} comparable to those of composites with coated fibers and dense matrices.¹¹ Furthermore, the mechanisms that lead to damage tolerance are essentially the same. That is, matrix cracks deflect at the fiber–matrix interfaces, fibers subsequently break in a stochastic (uncorrelated) manner, and, finally, the broken fibers pull out from the matrix, providing additional energy dissipation.

The principal objective of the present study is to probe the interfacial debonding and sliding properties in one family of porous-matrix oxide composites and begin to establish pertinent correlations with the state of the matrix. The study is based on a series of fiber push-in experiments on composites of Nextel 720 fibers and mullite/alumina matrices.¹⁰ To our knowledge, this represents the first study of its kind on this class of composite. It forms part of a broader effort to design and synthesize porous ceramics for use in oxide fiber composites.^{12,13} A secondary objective is to present a variant on the established fiber push-in technique¹⁴ and the associated analysis for use with porous

matrix composites. The variations include the use of a blunt (sphero-conical) indenter for push-in (rather than a sharp-tipped one) and the analysis of the hysteresis loop width to infer both the debond toughness and the interface sliding stress. The advantages and limitations of the method are highlighted.

II. Test Protocol and Analysis

The benchmark for measuring interface properties in ceramic composites is the fiber push-in test, introduced originally by Marshall and Oliver.¹⁴ Briefly, the test is performed by pushing an individual fiber into a composite using an instrumented indenter and measuring the resulting force–displacement response. The indenter tip is sharp so that the fiber undergoes plastic deformation during the test. To ascertain the sliding displacement from the measured displacement, an additional test on a reference (non-sliding) fiber is required. The reference state is produced in one of two ways. When the fiber coating is oxidizable, the composite is heat treated to remove the coating and to bond the matrix to the fibers.^{14,15} Otherwise, the reference state is achieved by fabricating a composite without a fiber coating and subjecting it to a heat treatment that produces strong interfacial bonds. In both cases, the sliding displacement is obtained by subtracting the displacements of the reference fiber from those of the sliding fiber at prescribed forces. The variation in sliding displacement with force is then analyzed in terms of an appropriate micromechanical model.

As the composites of current interest do not rely on the use of a fiber coating to effect debonding, neither one of the preceding techniques for producing a reference fiber is practical. A further complication arises from the low modulus of the porous matrices. That is, during fiber push-in, the surrounding matrix undergoes an indeterminate amount of elastic shear displacement, concurrent with the plastic displacement of the fiber surface and the sliding displacement. An illustrative example of this phenomenon is presented in Fig. 1. The results in the figure are based on finite element calculations of an axisymmetric unit cell model of a fiber composite, loaded uniformly over a circular patch concentric with the fiber. They demonstrate that the total elastic displacement δ at the center of the loading point increases appreciably with decreasing matrix modulus. For instance, δ triples as the matrix modulus is reduced from 260 GPa (that of Nextel 720 fibers)¹⁶ to 10 GPa (representative of the more compliant matrix used in the present study).¹³ One consequence is that, if the reference fibers were embedded in a dense matrix, the test results on these fibers would not capture all of the extraneous displacement. In light of these problems, a variant of the established push-in technique was developed and used in the present study, as described below.

The preceding problem of determining the sliding displacement can be obviated by implementing two changes: (i) using a blunt indenter that produces only elastic deformation of the fiber over the force range of interest (Fig. 2); and (ii) using the hysteresis loop width for analysis, rather than the absolute displacements during loading or unloading. The loop width is obtained by subtracting the measured displacements on loading and unloading at each force level; as the extraneous displacements are elastic, their values depend only on force and hence they cancel when the displacement difference is calculated.

G. Pharr—contributing editor

Manuscript No. 21367. Received January 10, 2006; approved May 2, 2006.

This work was funded by the Air Force Office of Scientific Research (award number F49550-05-1-0134), monitored by Dr. B. L. Lee. Funding for the nanoindenter was provided by the Defense University Research Instrumentation Program, also through the Air Force Office of Scientific Research (award number F49620-02-01-0292).

[†]Author to whom correspondence should be addressed. e-mail: zok@engineering.ucsb.edu

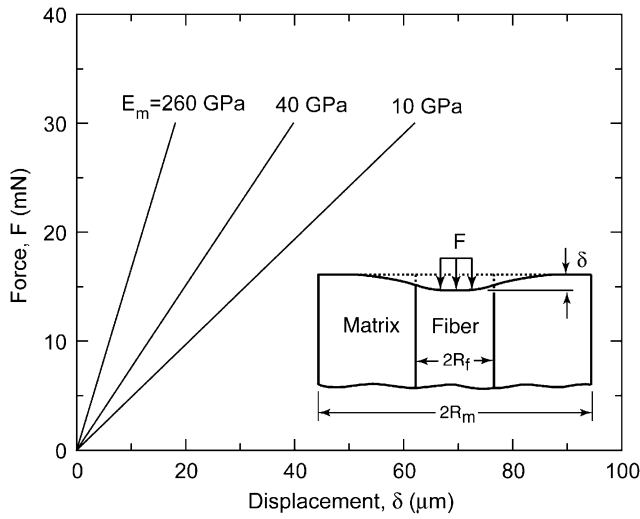


Fig. 1. Finite-element simulations of the elastic response of a composite during fiber push-in. Force applied over a circular area of radius $R_f/2$. Unit cell length is $L = 20R_m$. Other parameter values: $2R_f = 10 \mu\text{m}$, $2R_m = 25 \mu\text{m}$, $E_f = 260 \text{ GPa}$, $\nu_f = 0.2$, $\nu_m = 0.1$.

The loop width is analyzed using the shear lag model of Marshall and Oliver.¹⁴ The key assumption is that the interface is characterized by a debond toughness Γ and a constant sliding stress τ . The sliding displacement δ is then obtained from a shear lag analysis. Four solution domains exist. (i) Provided $\Gamma \neq 0$, sliding is initiated at a critical force F_C :

$$F_C = 2\pi\sqrt{R^3 E_f \Gamma} \quad (1)$$

where R is the fiber radius and E_f is the fiber Young's modulus. Below this force, $\delta = 0$. (ii) After the onset of debonding ($F > F_C$), the displacement δ_L during loading on the first cycle is given by

$$\delta_L = \frac{F^2}{4\pi^2 R^3 \tau E_f} - \frac{\Gamma}{\tau} \quad (2)$$

(iii) Upon unloading from the force maximum F_M , it follows that:

$$\delta_U = \delta_M \left(1 - \frac{1}{2} \left[1 - \frac{F}{F_M} \right]^2 \right) - \frac{\Gamma}{\tau} \quad (3)$$

with δ_M being the maximum displacement, evaluated from Eq. (2) at $F = F_M$. (iv) Then, during reloading (at the start of the second loading cycle), the displacement is

$$\delta_R = \frac{\delta_M}{2} \left(1 + \frac{F}{F_M} \right) - \frac{\Gamma}{\tau} \quad (4)$$

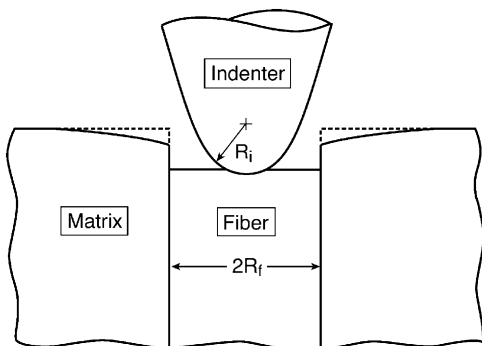


Fig. 2. Schematic of the fiber push-in test using a sphero-conical indenter.

Thereafter, upon further unloading and reloading between 0 and F_M , the displacements are again given by Eqs. (3) and (4).

Equations (1)–(4) lead directly to solutions for loop width: denoted Δ_1 for the first cycle and Δ_n for all subsequent cycles. Expressed in non-dimensional form, the results are

$$\frac{\Delta_1}{\Delta_*} = (1 - \gamma) \left(1 - \frac{1}{2} (1 - k)^2 \right) \quad (F < F_C) \quad (5a)$$

$$\frac{\Delta_1}{\Delta_*} = \frac{1}{2} + k - \frac{3k^2}{2} \quad (F > F_C) \quad (5b)$$

$$\frac{\Delta_n}{\Delta_*} = k(1 - k) \quad (5c)$$

where Δ_* is a reference displacement, defined by

$$\Delta_* \equiv \frac{F_M^2}{4\pi^2 R^3 \tau E_f} \quad (6a)$$

γ is a normalized toughness,

$$\gamma \equiv \frac{4\pi^2 \Gamma R^3 E_f}{F_M^2} \quad (6b)$$

and k is the normalized force,

$$k \equiv \frac{F}{F_M} \quad (6c)$$

Some representative numerical results are plotted in Fig. 3. They illustrate that the effects of γ are obtained only in the first loading cycle in the domain $F < F_C$. Thereafter, for $F > F_C$ in the first cycle and over the entire loading range for all subsequent cycles, the loop width is independent of γ .

Based on these observations, the following protocol has been established to determine Δ_* and γ from experimental measurements. From the first loop, the results at high forces ($F > F_C$) are fit by Eq. (5b) to ascertain Δ_* . Then, to obtain γ , the results at low force ($F < F_C$, also in the first loop) are fit by Eq. (5a), using the inferred value of Δ_* . From Eqs. (6a) and (6b) and the known values of R and E_f , the values of τ and Γ are computed. For subsequent loading cycles, Eq. (5c) is used to fit the data and infer the values of Δ_* and τ .

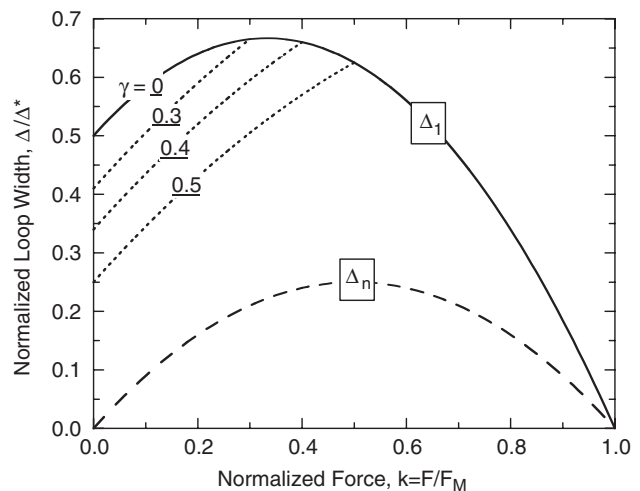


Fig. 3. Variation in loop width with applied force for the first and subsequent loading cycles. The dotted lines are from Eq. (5a) ($F < F_C$) and the solid lines from Eq. (5b) ($F > F_C$); both are for the first loading/unloading excursion. The dashed line is from Eq. (5c) and corresponds to all subsequent loading cycles.

III. Materials and Testing Procedures

The composites were comprised of a Nextel 720 fiber cloth in an 8-harness satin weave and a porous matrix of mullite and alumina. The processing route has been described in detail in earlier articles.^{4,9} Briefly, the matrix was introduced in two steps: (i) vacuum infiltration of a slurry containing 80% mullite and 20% alumina particles into the fiber preform, and (ii) impregnation and pyrolysis of an alumina precursor solution ($\text{Al}_2\text{Cl}(\text{OH})_5$). The volumetric yield of the precursor solution upon conversion to γ -alumina was 6.4%. After drying, the panels were fired at 900°C for 2 h, thereby converting the precursor to γ -alumina. After all impregnation cycles were completed, the panels were given a final heat treatment at 1200°C for 2 h. In the latter step, the γ -alumina is converted to α -alumina. The average fiber volume fraction was 38%. Two different composites were tested, distinguished by the number of precursor impregnation and pyrolysis (PIP) cycles: 0 or 2, subsequently referred to as 0 PIP and 2 PIP. In preparation for push-in testing, samples were impregnated with a low-viscosity epoxy and polished to a 0.1 μm finish. The epoxy was then burned out at 550°C for 2 h.

Push-in tests were performed using an instrumented Hysitron Triboindenter (Hysitron Inc., Minneapolis, MN). The loading head has a force resolution of 1 nN, a displacement resolution of 0.4 nm, and a force capacity of 30 mN. Additionally, it is capable of acting as a scanning probe microscope (SPM). Specimens were placed in the instrument chamber several hours before testing to allow thermal equilibration. Immediately before each test, the thermal drift rate was measured and used subsequently to correct the measured displacements. All tests were performed with a diamond sphero-conical indenter with a tip radius $R_i = 5 \mu\text{m}$. Preliminary tests at varying peak forces coupled with SPM images before and after testing revealed that there was no detectable plastic deformation of the fibers up to the maximum possible force (30 mN). Consequently, all subsequent tests were performed to this level. Push-in tests were performed by placing the indenter at the center of the targeted fiber, loading at a rate of 15 mN/s to the maximum, and unloading at the same rate. Each tested fiber was subjected to three loading-unloading cycles. To account for spatial variations, fibers were selected from multiple bundles within each test specimen. The radii of tested fibers were measured from the SPM images.

IV. Measurements and Analysis

Representative force-displacement curves from the first two loading cycles for the 0 PIP material are plotted in Fig. 4. Similar curves were obtained for the 2 PIP material. Analyses of the test results via the protocol described in Section II yielded the results in Fig. 5. For the first loading cycle for both materials, the extrapolated curve from the high force domain to lower

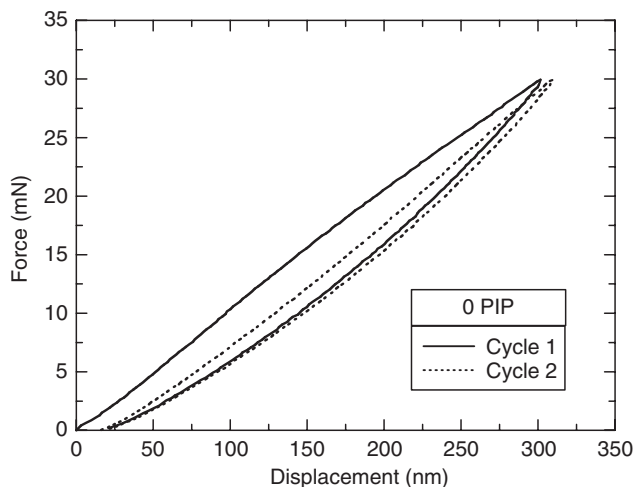


Fig. 4. Typical force-displacement curves from a fiber push-in test.

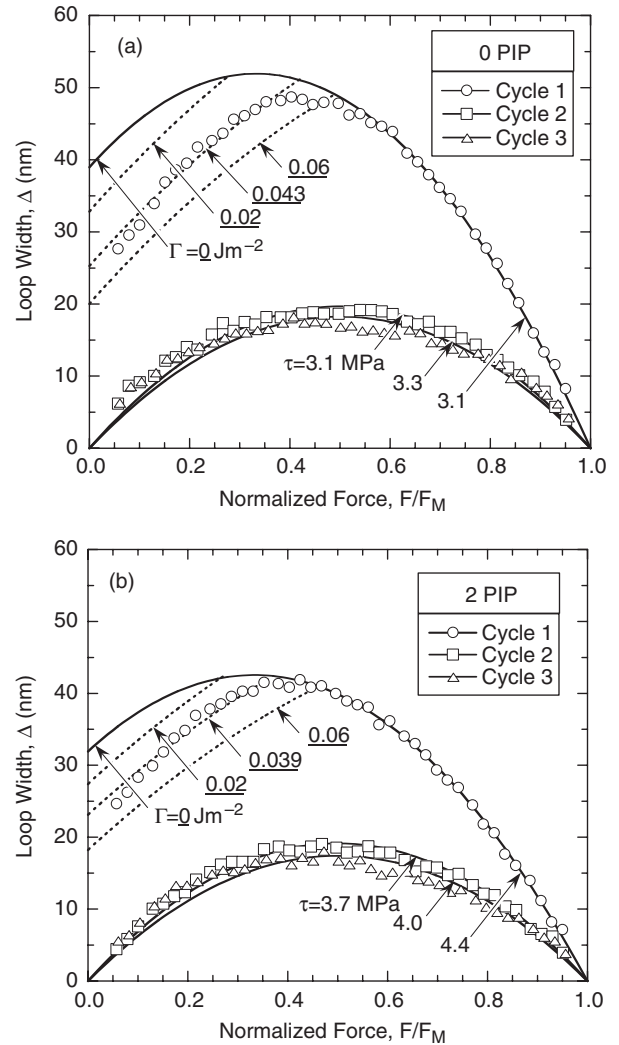


Fig. 5. Representative measured loop width curves for (a) 0 PIP and (b) 2 PIP materials. Also shown are the fit curves used to obtain Γ and τ .

forces yielded loop widths that were greater than the measured values. The inference is that the debond energy is finite. Examples of the parametric studies used to infer Γ from the low force domain are also shown in Fig. 5. Although a rigorous error analysis was not performed, visual inspections of the best-fit curves and those from off-optimal fits indicated an uncertainty of about 10% in both Γ and τ from an individual curve. The shapes of the curves for the second and third loops were consistent with those predicted by the model, assuming a constant interfacial sliding stress (Eq. (5c)). Here, again, the uncertainty in the inferred value of τ was about 10%.

Distributions in the sliding stresses from individual tests and their average values are summarized in Figs. 6 and 7. For each of the two materials and each of the three loading cycles, the results span a wide range: typically 2–12 MPa. But the average values for the first loading cycle differ only slightly between the two materials: 4.8 ± 0.5 and 5.9 ± 0.5 MPa for 0 PIP and 2 PIP, respectively. For subsequent loading cycles ($N = 2$ and 3), the values are essentially the same, lying between 4.2 and 4.6 MPa for both materials. The inferred values of Γ (Fig. 8) follow similarly broad distributions (0.01–0.1 J/m^2) and their averages exhibit only a weak sensitivity to the number of precursor impregnation cycles: 0.04 ± 0.02 and $0.05 \pm 0.02 \text{ J/m}^2$ for 0 PIP and 2 PIP, respectively.

V. Discussion and Conclusions

The debond toughness in the present composites is insensitive to the state of the matrix and is about an order of magnitude lower

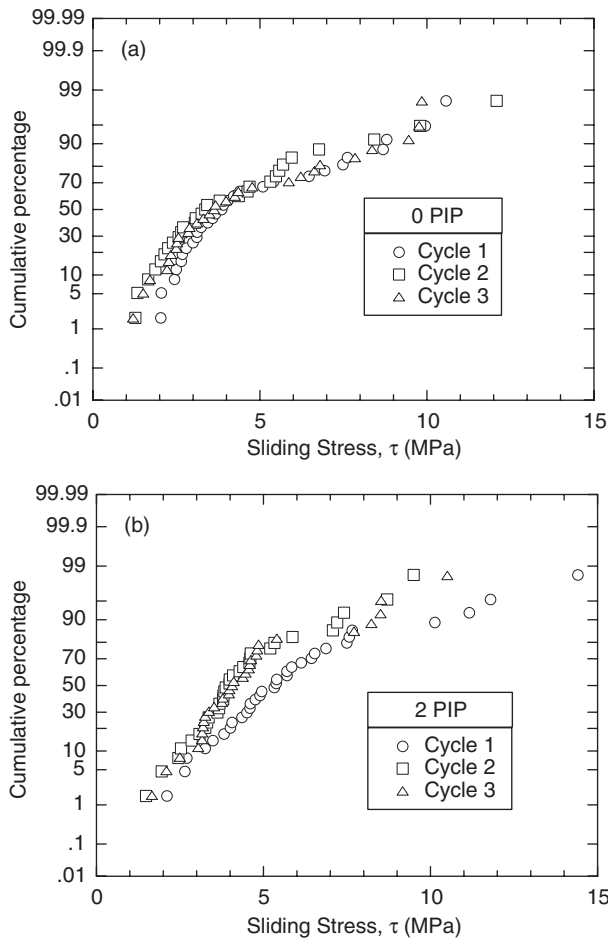


Fig. 6. Distributions of sliding stress for (a) 0 PIP and (b) 2 PIP composites.

than the toughness of the matrix alone: the latter falling in the range 1–3 J/m².¹³ The latter result differs from the expectation that, because of similar compositions of the matrix and the fibers (both being mullite/alumina mixtures), the two toughnesses should be comparable to one another. The disparity can be attributed at least in part to the reduced packing efficiency of matrix particles near the fiber surface relative to that in the bulk.¹⁷ More importantly, the debond toughness is about two orders of magnitude lower than the fiber toughness, Γ_f . The corresponding ratio, Γ/Γ_f , falls well within the domain in which matrix

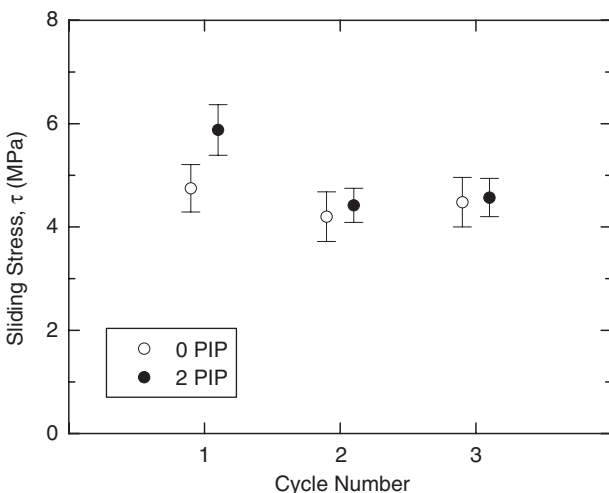


Fig. 7. Effects of number of loading cycles on the sliding stress (error bars represent standard deviations of the mean).

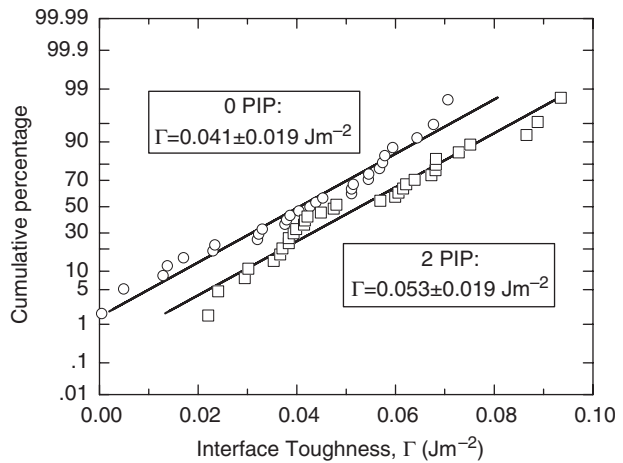


Fig. 8. Distributions of interface toughness.

cracks are predicted to deflect into the interface rather than penetrate into the fibers.¹⁸ This result is consistent with the observed fiber pullout on tensile fracture surfaces of these composites.¹⁰

The measured sliding stresses coincide remarkably closely with those measured in Nicalon/LAS composites with C coatings on the fibers (also in the range 2–12 MPa).¹⁵ This result, in combination with the low debond toughness, appears qualitatively consistent with the similarities in the damage tolerance of the two systems, as manifested in the degree of notch sensitivity of tensile strength.¹¹

From a testing perspective, the current push-in method has three advantages over the one developed by Marshall and Oliver.¹⁴ (i) It mitigates the problem associated with the elastic displacement of the matrix: an important factor in the testing of porous matrix composites; (ii) measurements of the indentation response of a reference fiber are unnecessary, making test implementation easier; and (iii) as all measurements used for analysis come directly from a single fiber, the accuracy of measurements is likely higher. These benefits are offset by two limitations. (i) The analysis is predicated on the assumption that the sliding stress is the same for both forward and reverse loading. Although this appears to be a reasonable assumption, a critical assessment can only be made by separately analyzing loading and unloading portions of push-in curves. (ii) The analysis is also predicated on the fiber response being purely elastic. That is, the maximum force must not exceed that for fiber yielding. Otherwise, the hysteretic displacements due to fiber plasticity must be taken into account. This problem was not encountered in the present study.

A guide to the allowable maximum force can be obtained from Hertzian contact mechanics. The critical force, F_y , for yield initiation is^{19,20}:

$$\frac{F_y}{R_i^2} = C \left(\frac{H_f^3 (1 - \nu_f^2)^2}{E_f^2} \right) \left(1 + \frac{E_f (1 - \nu_f^2)}{E_i (1 - \nu_f^2)} \right)^2 \quad (7)$$

where $C \approx 0.8$, R_i is the indenter tip radius, H is hardness, E is Young's modulus, ν is Poisson's ratio, and the subscripts f and i refer to the fiber and the indenter, respectively. Plasticity initiates at a point about $a/2$ beneath the surface (a being the contact radius) and subsequently expands and approaches the free surface with increasing force. While contained within the sub-surface region, the plastic strains remain small (comparable to the elastic strains of the surrounding material) and the macroscopic response is essentially indistinguishable from that of an elastic material. Only when the plastic zone reaches the free surface does the plasticity begin to develop in full earnest, leaving a detectable permanent impression after unloading.²¹ The critical force for this transition depends on the material

yield strain and work hardening characteristics, but is typically of order $5F_y$. A key implication is that, as $F_y \propto R^2$, the onset of yielding can be delayed by using an indenter with a larger tip radius, thereby extending the elastic domain to higher force levels.

References

- ¹W. C. Tu, F. F. Lange, and A. G. Evans, "Concept for a Damage-Tolerant Ceramic Composite with Strong Interfaces," *J. Am. Ceram. Soc.*, **79** [2] 417–24 (1996).
- ²C. G. Levi, J. Y. Yang, B. J. Dalgleish, F. W. Zok, and A. G. Evans, "Processing and Performance of an All-Oxide Ceramic Composite," *J. Am. Ceram. Soc.*, **81** [8] 2077–86 (1998).
- ³V. A. Krumb, R. John, and L. P. Zawada, "Notched Fracture Behavior of an Oxide/Oxide Ceramic-Matrix Composite," *J. Am. Ceram. Soc.*, **82** [11] 3087–96 (1999).
- ⁴J. A. Heathcote, X.-Y. Gong, J. Yang, U. Ramamurty, and F. W. Zok, "In-Plane Mechanical Properties of an All-Oxide Ceramic Composite," *J. Am. Ceram. Soc.*, **82** [10] 2721–30 (1999).
- ⁵C. G. Levi, F. W. Zok, J.-Y. Yang, M. Mattoni, and J. P. A. Lofvander, "Microstructural Design of Stable Porous Matrices for All-Oxide Ceramic Composites," *Z. Metallkd.*, **90** [12] 1037–47 (1999).
- ⁶S. C. Jurf and R. A. Butner, "Advances in Oxide-Oxide CMC," *J. Eng. Gas Turb. Power*, **122** [2] 202–5 (2000).
- ⁷B. Kanka and H. Schneider, "Aluminosilicate Fiber/Mullite Mullite Composites with Favorable High-Temperature Properties," *J. Eur. Ceram. Soc.*, **20** [14–15] 619–23 (2000).
- ⁸V. A. Krumb, R. John, and D. A. Stubbs, "A Study of the Damage Progression from Notches in an Oxide/Oxide Ceramic-Matrix Composite Using Ultrasonic C-Scans," *Comp. Sci. Technol.*, **61** [11] 1561–70 (2001).
- ⁹M. Mattoni, J. Y. Yang, C. G. Levi, and F. W. Zok, "Effects of Matrix Porosity on the Mechanical Properties of a Porous-Matrix, All-Oxide Ceramic Composite," *J. Am. Ceram. Soc.*, **84** [11] 2594–602 (2001).
- ¹⁰M. A. Mattoni and F. W. Zok, "Strength and Notch Sensitivity of Porous-Matrix Oxide Composites," *J. Am. Ceram. Soc.*, **88** [6] 1504–13 (2005).
- ¹¹F. W. Zok, "Fracture Analysis of Fiber-Reinforced Ceramic Composites"; pp. 407–18 in *ASM International Engineered Materials Handbook, Vol. 1: Composites*, 2nd edition, ASM International, Material Park, OH, 2001.
- ¹²H. Fujita, G. Jefferson, R. M. McMeeking, and F. W. Zok, "Mullite-Alumina Mixtures for Use as Porous Matrices in Oxide Fiber Composites," *J. Am. Ceram. Soc.*, **87** [2] 261–7 (2004).
- ¹³H. Fujita, G. Jefferson, C. G. Levi, and F. W. Zok, "Controlling Mechanical Properties of Porous Mullite/Alumina Mixtures Via Precursor-Derived Alumina," *J. Am. Ceram. Soc.*, **88** [2] 367–75 (2005).
- ¹⁴D. B. Marshall and W. C. Oliver, "Measurement of Interfacial Mechanical Properties in Fiber-Reinforced Ceramic Composites," *J. Am. Ceram. Soc.*, **70** [8] 542–8 (1987).
- ¹⁵T. P. Weihs and W. D. Nix, "Experimental Examination of the Push-Down Technique for Measuring the Sliding Resistance of Silicon Carbide Fibers in a Ceramic Matrix," *J. Am. Ceram. Soc.*, **74** [3] 524–34 (1991).
- ¹⁶D. M. Wilson, "Statistical Tensile Strength of Nextel 610 and Nextel 720 Fibres," *J. Mater. Sci.*, **32** [10] 2535–42 (1997).
- ¹⁷F. W. Zok, F. F. Lange, and J. R. Porter, "Packing Density of Composite Powder Mixtures," *J. Am. Ceram. Soc.*, **74** [8] 1880–5 (1991).
- ¹⁸M.-Y. He and J. W. Hutchinson, "Crack Deflection at an Interface Between Dissimilar Elastic Materials," *Int. J. Solids Struct.*, **25** [9] 1053–67 (1989).
- ¹⁹K. L. Johnson, *Contact Mechanics*. Cambridge University Press, Cambridge, U.K., 1985.
- ²⁰B. Bhushan, *Principles and Applications of Tribology*. John Wiley & Sons, New York, 1999.
- ²¹Y. J. Park and G. M. Pharr, "Nanoindentation with Spherical Indenters: Finite Element Studies of Deformation in the Elastic-Plastic Transition Regime," *Thin Solid Films*, **246**, 447–8 (2004). □